Inorg. Chem. **2001,** *40,* 3656−3669

Invited Award Contribution for ACS Award in Inorganic Chemistry

Geometric and Electronic Structure Contributions to Function in Bioinorganic Chemistry: Active Sites in Non-Heme Iron Enzymes

Edward I. Solomon[†]

Department of Chemistry, Stanford University, Stanford, California 94305-5080

Received March 29, 2001

Spectroscopy has played a major role in the definition of structure/function correlations in bioinorganic chemistry. The importance of spectroscopy combined with electronic structure calculations is clearly demonstrated by the non-heme iron enzymes. Many members of this large class of enzymes activate dioxygen using a ferrous active site that has generally been difficult to study with most spectroscopic methods. A new spectroscopic methodology has been developed utilizing variable temperature, variable field magnetic circular dichroism, which enables one to obtain detailed insight into the geometric and electronic structure of the non-heme ferrous active site and probe its reaction mechanism on a molecular level. This spectroscopic methodology is presented and applied to a number of key mononuclear non-heme iron enzymes leading to a general mechanistic strategy for O_2 activation. These studies are then extended to consider the new features present in the binuclear non-heme iron enzymes and applied to understand (1) the mechanism of the two electron/coupled proton transfer to dioxygen binding to a single iron center in hemerythrin and (2) structure/function correlations over the oxygen-activating enzymes stearoyl-ACP Δ^9-desaturase, ribonucleotide reductase, and methane monooxygenase. Electronic structure/reactivity correlations for O_2 activation by non-heme relative to heme iron enzymes will also be developed.

Introduction

I am a physical inorganic chemist interested in the application of a wide range of spectroscopic methods to define the electronic structure of transition metal complexes and understand this contribution to physical properties and reactivity. Many of the complexes we study are unusual inorganic complexes in that they are active sites in catalysis. This presentation focuses on the non-heme iron enzymes involved in dioxygen activation. These comprise a large area in bioinorganic chemistry that had generally not been accessible through traditional spectroscopic approaches. The development of a new spectroscopic method, variable temperature, variable field magnetic circular dichroism (VTVH MCD) of non-Kramers ions,[1] has now enabled us to study these systems in detail on a molecular level and generate new insights into geometric and electronic structure contributions to reactivity in bioinorganic chemistry.[2] We first consider the mononuclear non-heme iron enzymes and then extend the methodology to the binuclear iron metalloproteins. For each system we consider the electronic structure of the oxygen intermediates generated and how this contributes to activation for catalysis.

Mononuclear Non-Heme Iron Enzymes

Table 1 gives a partial list of the mononuclear non-heme iron enzymes we study at Stanford. These catalyze a wide range of reactions including dioxygenation, hydroxylation, four-electron oxidation, and H-atom abstraction. This range is as extensive as in heme chemistry, and as with heme systems these reactions for the most part involve dioxygen activation by high-spin ferrous sites. However, the non-heme iron enzymes are much more difficult to study than heme systems in that they do not have intense porphyrin-based electronic transitions. In addition, high-spin ferrous active sites do not exhibit the intense charge-transfer transitions of ferric centers and the d^6 configuration gives an $S = 2$ integer spin ground state which is usually inaccessible by electron paramagnetic resonance (EPR)-based methods. Thus we have developed a spectroscopic methodology, near-IR VTVH MCD, to study these non-Kramers ions, and this will be presented in the next section. The pterin-dependent non-heme iron enzyme phenylalanine hydroxylase will then be used as an example that demonstrates the molecular level mechanistic insight obtained from this spectroscopic approach. Parallel studies over many members of this class have led to a

---

[†] E-mail: edward.solomon@stanford.edu.

(1) Solomon, E. I.; Pavel, E. G.; Loeb, K. E.; Campochiaro, C. *Coord. Chem. Rev.* **1995**, *144*, 369−460.

(2) Solomon, E. I.; Brunold, T. C.; Davis, M. I.; Kemsley, J. N.; Lee, S.-K.; Lehnert, N.; Neese, F.; Skulan, A. J.; Yang, Y.-S.; Zhou, J. *Chem. Rev.* **2000**, *100*, 235−349.

10.1021/ic010348a CCC: $20.00

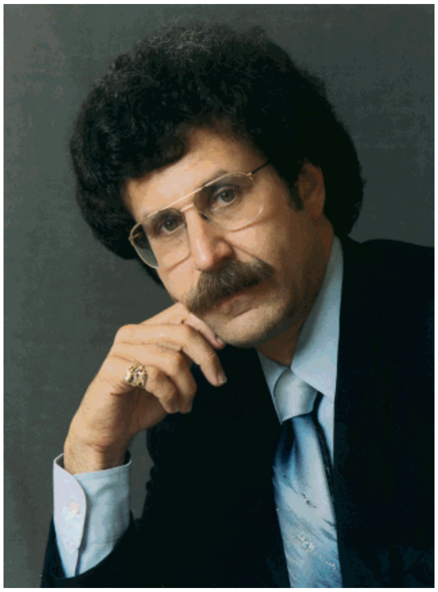

Edward I. Solomon grew up in North Miami Beach, FL, received his Ph.D. from Princeton University (with D. S. McClure), and was a postdoctoral fellow at the H. C. Ørsted Institute (with C. J. Ballhausen) and then at Caltech (with H. B. Gray). He was a professor at MIT until 1982. He then moved to Stanford University, where he is now the Monroe E. Spaght Professor of Humanities and Sciences. His research is in the fields of physical–inorganic and bioinorganic chemistry with emphasis on the application of a wide variety of spectroscopic methods to elucidate the electronic structures of transition-metal complexes and their contributions to physical properties and reactivity. He has presented numerous named lectures including the First Glenn Seaborg Lectures at U. C. Berkeley, and has been an invited professor at the Tokyo Institute of Technology, Japan; University of Paris, Orsay, France; Tata Institute, Bombay, India; Xiamen University, China; and La Plata University, Argentina. He is a Fellow of the American Academy of Arts and Sciences and the American Association for the Advancement of Sciences and has received a range of awards including the Ira Remsen Award from the Maryland section of the American Chemical Society, the G. W. Wheland Medal from the University of Chicago, and the ACS Award in Inorganic Chemistry for 2001.

general mechanistic strategy for O_2 reactivity used by the non-heme iron enzymes. Reaction with dioxygen leads to oxygen intermediates of the non-heme iron site that, in the case of the anticancer drug bleomycin, can be trapped and studied in detail using a ferric spectroscopic approach (which combines VTVH MCD with zero field splitting (ZFS), resonance Raman (rR) profiles, and density functional theory (DFT) calculations).[3] These studies provide fundamental insight into non-heme relative to heme reactivity in dioxygen activation. In the second part of this presentation these studies are extended to the binuclear non-heme iron enzymes.

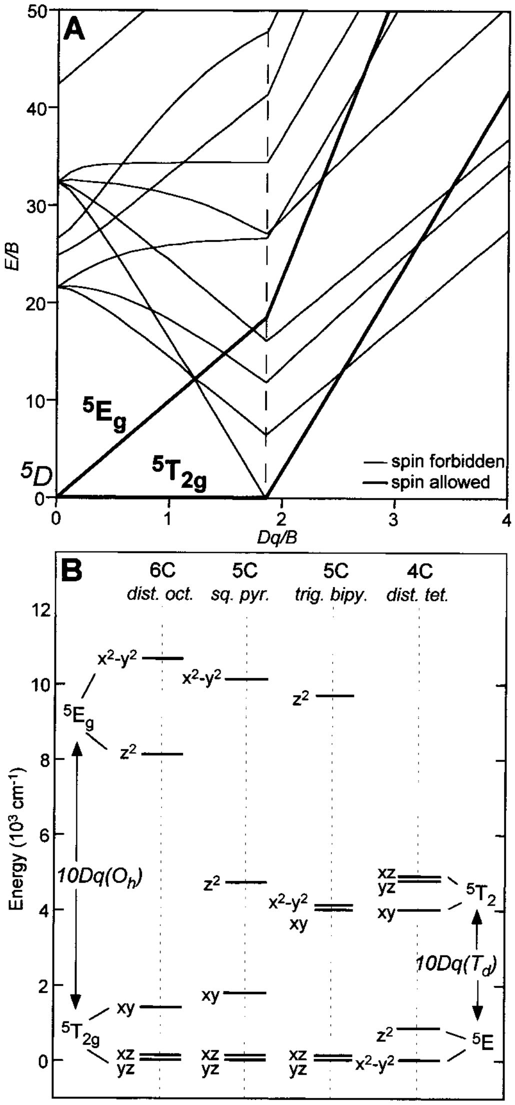

Figure 1. Fe^{II} ligand field theory. (A) d^6 Tanabe–Sugano diagram. (B) One-electron d-orbitals in different ligand fields. (Adapted from ref 2.)

VTVH MCD Methodology. The electronic structure of a high-symmetry Fe^{II} site is given by the d^6 Tanabe–Sugano diagram in Figure 1A. On the left is the high-spin $^5T_{2g}$, $S = 2$ ground state of relevance to the non-heme ferrous enzymes. While there are many possible excited states, only the ^5E_g is accessible through a spin-allowed transition from the quintet ground state. This is at an energy of $10Dq$, which for the non-heme relevant nitrogen and oxygen ligation is ~10000 cm^{-1}. Both the E and T_2 states are orbitally degenerate, and these will split in energy in the low-symmetry protein environment. This splitting is given by ligand field theory (Figure 1B).[1,2] For a distorted 6-coordinate site the ^5E will split by up to 2000 cm^{-1}, centered around 10000 cm^{-1}. If one ligand is removed to generate a square pyramidal 5-coordinate center, the ^5E splitting is large and leads to one transition at >10000 cm^{-1} and a second in the 5000 cm^{-1} region. Rearrangement of the five ligands into a trigonal bipyramidal structure changes the ligand field and shifts the excited states to below 10000 and below 5000 cm^{-1}. Finally, for a 4-coordinate distorted tetrahedral structure, $10Dq(T_d) \approx (-4/9)10Dq(O_h)$ and there will be excited states only in the low-energy region. It should be observed from Figure 1B that the T_{2g} ground-state degeneracy will also split in energy in low-symmetry geometries, and we will return to this splitting below. The energies of the ^5E excited state are thus sensitive probes of the coordination environment at a ferrous active site. However, transitions to these excited states will be weak in absorption since they are Laporté forbidden. In addition, these will be in the 12000–5000 cm^{-1} near-IR spectral region and will be obscured by vibrations and overtones of the protein and buffered solvent. However, the ground state of a high-spin ferrous site is $S = 2$ and paramagnetic. Paramagnetic centers show *C*-term behavior in the MCD spectrum that increases in intensity as temperature decreases (vide infra),[4,5] and at low temperatures the signal is orders of magnitude more intense than

---

(3) Lehnert, N.; DeBeer George, S.; Solomon, E. I. *Curr. Opin. Chem. Biol.* **2001**, *5*, 165–167.

Table 1. Mononuclear Non-Heme Iron Enzymes

Reaction Type	Representative Enzyme	Catalytic Reaction
intradiol dioxygenation	protocatechuate 3,4-dioxygenase	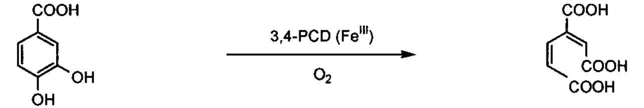 3,4-PCD (Fe^{III}) O_2
extradiol dioxygenation	catechol 2,3-dioxygenase	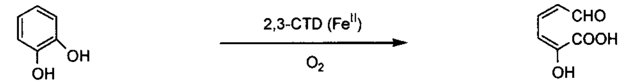 2,3-CTD (Fe^{II}) O_2
hydroperoxidation	lipoxygenases	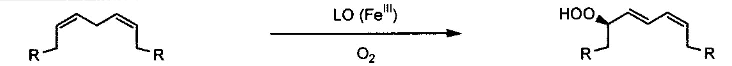 LO (Fe^{III}) O_2
cis-hydroxylation	phthalate dioxygenase	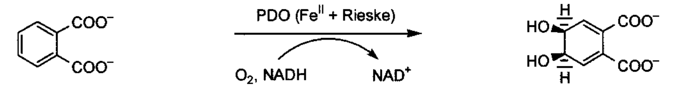 PDO (Fe^{II} + Rieske) O_2, NADH NAD$^+$
⇨ pterin-dependent hydroxylation	phenylalanine hydroxylase	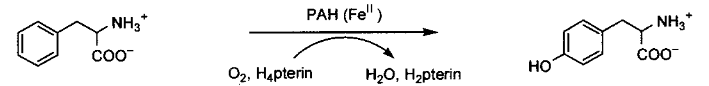 PAH (Fe^{II}) O_2, H_4pterin H_2O, H_2pterin
α-ketoglutarate-dependent hydroxylation	clavaminate synthase	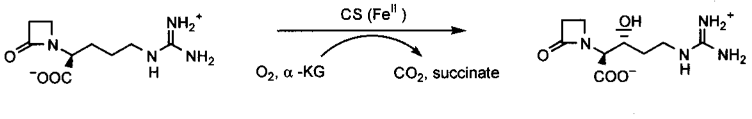 CS (Fe^{II}) O_2, α -KG CO_2, succinate
α-ketoglutarate-dependent 4e$^-$ oxidation	clavaminate synthase	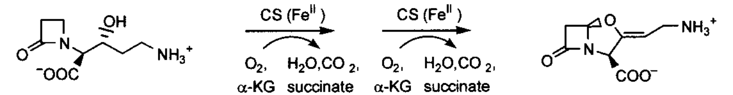 CS (Fe^{II}) CS (Fe^{II}) O_2, α-KG H_2O,CO_2, succinate O_2, α-KG H_2O,CO_2, succinate
⇨ H• abstraction	bleomycin	*DNA* $\xrightarrow[O_2]{\text{BLM (Fe}^{II})}$ *base propenals*

the diamagnetic background. Thus, the way to spectroscopically study non-heme ferrous active sites is through near-IR MCD at low temperature.

The predictions of ligand field theory in Figure 1B have been evaluated and supported experimentally using MCD spectroscopy to study 25 structurally defined non-heme ferrous model complexes.[6] As shown in Figure 2, distorted 6-coordinate complexes exhibit two ligand field transitions (corresponding to the two components of the ^5E_g excited state in Figure 1B) in the 10000 cm^{-1} region split by $<$2000 cm^{-1}. Square pyramidal complexes exhibit one ligand field transition at $>$10000 cm^{-1} and a second transition in the 5000 cm^{-1} energy region. For trigonal bipyramidal sites the transition energies are below 10000 and 5000 cm^{-1}, and 4-coordinate distorted tetrahedral ferrous complexes exhibit only low-energy ligand field transitions in the 6000 cm^{-1} region.

We now focus on the energy splitting of the $^5T_{2g}$ ground state (Figure 1B), which can be obtained from the VTVH behavior of the MCD spectrum. Figure 3A shows that the MCD signal at low temperature increases with increasing magnetic field. This is plotted in the saturation magnetization curve in Figure 3B (MCD intensity vs $\beta H/2kT$). Note that the MCD intensity first increases with increasing magnetic field and decreasing temperature (as H/T) but then levels off (i.e., saturates) at high magnetic field and low temperature. This behavior can be easily understood using the simple case of an $S = {}^1/_2$ Kramers doublet (Figure 3B inset).[1,2] Both the ground and excited states Zeeman split by $g\beta H$ in a magnetic field. As shown in the inset, two transitions of equal magnitude but opposite sign are predicted to a given excited state. These mostly cancel at high temperature, but as the temperature is decreased the $M_S = -{}^1/_2$ component of the ground state is selectively Boltzmann populated, cancellation no longer occurs, and the MCD signal increases (as 1/*T*

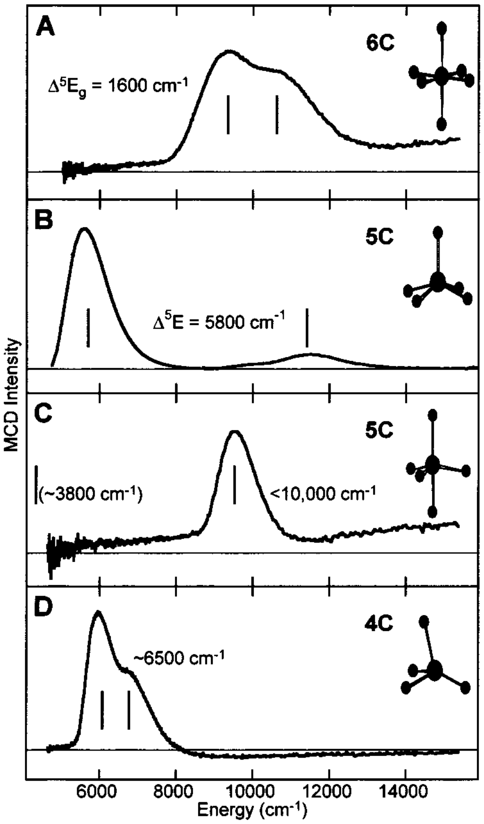

Figure 2. Low-temperature MCD spectra of representative Fe^{II} model complexes. (Adapted from refs 2 and 6.)

---

(4) Piepho, S. B.; Schatz, P. N. *Group Theory in Spectroscopy: With Applications to Magnetic Circular Dichroism*; Wiley: New York, 1983.

(5) Stephens, P. J. *Adv. Chem. Phys.* **1976**, *35*, 197−264.

(6) Pavel, E. G.; Kitajima, N.; Solomon, E. I. *J. Am. Chem. Soc.* **1998**, *120*, 3949−3962.

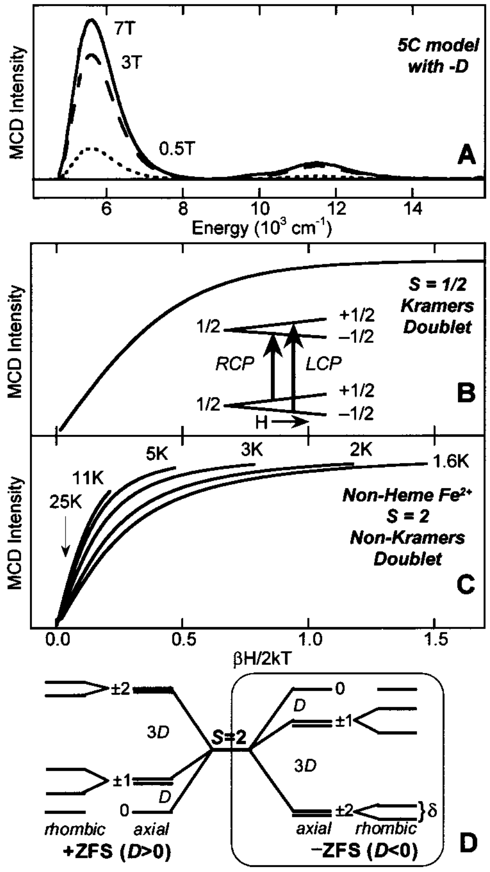

Figure 3. VTVH MCD. (A) Field dependence of the MCD spectrum for a 5-coordinate (5C) model with negative ZFS. (B) Saturation magnetization curve for an $S = {}^1/_2$ Kramers doublet. Inset gives CD selection rules in a longitudinal magnetic field. (C) Nested saturation magnetization curves for an $S = 2$ non-Kramers doublet. (D) Energy splittings of the $S = 2$ sublevels for positive ZFS (left) and negative ZFS (right). (Adapted from refs 1, 2, and 10.)

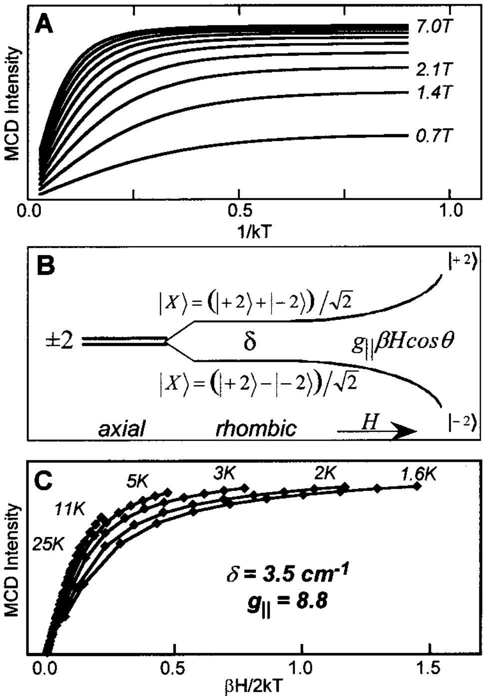

Figure 4. Saturation behavior of non-Kramers doublets. (A) Saturation data from Figure 3C replotted as a function of $1/kT$ for fixed magnetic fields. (B) Rhombic and magnetic field splitting and mixing of an $M_S = \pm 2$ non-Kramers doublet. (C) Theoretical fit to experimental data for 5-coordinate (5C) model with negative ZFS. (Adapted from refs 1, 2, and 10.)

resulting in a *C*-term). However, at high field and low temperature only the $M_S = -{}^1/_2$ component of the ground state is populated and at this point the MCD signal is saturated; it can no longer increase with increasing magnetic field or decreasing temperature. When the variable field MCD experiment is performed on an $S = {}^1/_2$ Kramers system at different temperatures, all the data superimpose on one $\beta H/2kT$ curve (Figure 3B), which is the Brillouin function for an $S = {}^1/_2$ system.[7] However, this is not the case for a non-heme ferrous site.[8] From Figure 3C, the saturation magnetization curves obtained at different temperatures are spread or nested.[9] This directly reflects the non-Kramers doublet nature of the $S = 2$ ground state,[1,7,8] which requires consideration of ZFS.

The $S = 2$ ground state is 5-fold degenerate in M_S (= 0, ±1, ±2). This degeneracy will split in energy even in the absence of a magnetic field if the ferrous site symmetry is lower than octahedral or tetrahedral. This energy splitting is given by the spin Hamiltonian in eq 1.

$$\mathcal{H} = D[S_z^2 - {}^1/_3S(S + 1)] + E(S_x^2 - S_y^2) \qquad (1)$$

For an axial system, $D \neq 0$, and when the ligand field along the axial direction is strong, D is positive. This produces the splitting pattern on the left of Figure 3D with the $M_S = 0$ at lowest energy. When the axial ligand field is weak, D is negative and the $M_S = \pm 2$ is lowest (Figure 3D, right). In a non-heme environment the rhombic term, E, is nonzero, and this splits the ±2 ground doublet by an amount δ (Figure 3D, far right). This splitting can only occur for non-Kramers ions, and when δ is large this leads to the lack of an EPR signal. It is also the origin of the nesting of the saturation magnetization MCD data in Figure 3C; hence analysis of these VTVH MCD data can provide a direct probe of the EPR inactive ground state.[8]

This can be seen from Figure 4A, which replots the data in Figure 3C so as to uncouple the magnetic field and temperature dependence. For a fixed field, as the temperature decreases the MCD signal first increases and then levels off indicating saturation of the lowest component of the ground state. Importantly, from Figure 4A the MCD signal intensity at low temperature saturation increases with increasing magnetic field in a nonlinear manner converging at high field. This indicates that the wave function of the ground state is changing with magnetic field. This is exactly the behavior of a ZFS non-Kramers doublet as shown in Figure 4B. At zero magnetic field, the $M_S = \pm 2$ sublevels are mixed as well as split in energy (by δ). When the field is turned on, in addition to the Zeeman splitting of these levels (by $g_{\|}\beta H$), the wave functions change and become pure −2 and +2 and thus MCD active at high fields. The non-Kramers doublet model in Figure 4B with appropriate orientation averaging for a frozen protein solution can be applied to fit the data in Figure 4C to evaluate the spin Hamiltonian parameters of the ground state (δ, $g_{\|}$ in Figure 4B). We are therefore using an excited state to probe the ground state and extracting EPR parameters from an EPR inaccessible active site.

We can then use these spin Hamiltonian parameters to derive the orbital splittings of the $^5T_{2g}$ ground state.[1] The T_{2g}

---

[7] Whittaker, J. W.; Solomon, E. I. *J. Am. Chem. Soc.* **1988**, *110*, 5329−5339.

[8] Whittaker, J. W.; Solomon, E. I. *J. Am. Chem. Soc.* **1986**, *108*, 835−836.

[9] Thomson, A. J.; Johnson, M. K. *Biochem. J.* **1980**, *191*, 411−420.

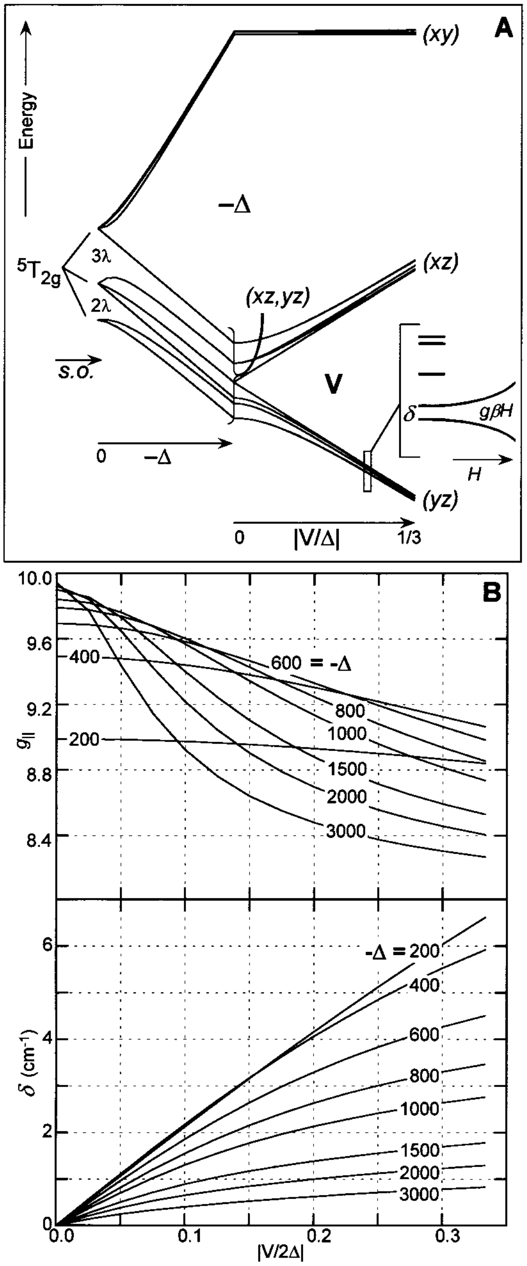

Figure 5. (A) Ligand field theory of $^5T_{2g}$ ground-state splitting, including in-state spin−orbit coupling. Inset at right shows expanded scale with non-Kramers doublet. (B) Relationship between δ and $g_{\|}$ and the ligand field parameters $-\Delta$ (axial splitting) and V (rhombic splitting) of the t_{2g} orbitals for a system with negative ZFS. (Adapted from refs 1 and 2.)

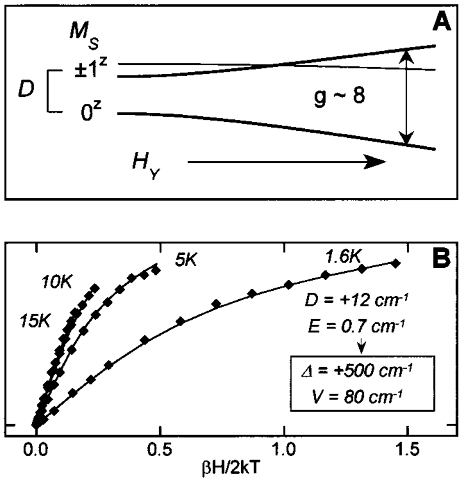

Figure 6. Positive ZFS. (A) Magnetic field splitting of a positive ZFS system with the field perpendicular to the *z*-axis. (B) *z*-Polarized saturation magnetization data for a $+D$ complex. (Adapted from refs 1, 2, and 10.)

corresponds to an extra electron in the *xy*, *yz*, or *xz* d-orbital. This produces an effective orbital angular momentum of $L' = 1$, which will spin−orbit couple to the quintet $S = 2$ and split the ferrous ground state even in an octahedral environment (far left in Figure 5A). This spin−orbit interaction will be similar for all ferrous sites. Lowering the symmetry of the ligand field produces an axial splitting of the *xy* relative to the (*xz*, *yz*) set given by the energy parameter Δ, and a rhombic splitting of the *xz* and *yz* orbitals by an amount V. The combined effects of spin−orbit coupling and low-symmetry t_{2g} orbital splittings are given to the right of Figure 5A, where the expanded scale shows that these produce the non-Kramers doublet ground state considered above. The spin Hamiltonian parameters δ and $g_{\|}$ can then be calculated as a function of the axial (Δ) and rhombic (V) splittings of the t_{2g} set of d-orbitals. The resultant plots in Figure 5B allow the experimental values of δ and $g_{\|}$ obtained from the VTVH MCD data (Figure 4C) to be used to obtain the t_{2g} orbital splitting.

The analysis in Figure 5 is appropriate for the case where the (*xz*, *yz*) set of d-orbitals is energetically below the *xy* orbital, which corresponds to a weak axial ligand field splitting and negative ZFS. In Figure 6 the methodology is extended to the positive ZFS case.[10] Figure 6B shows the experimental data for a ferrous model complex with positive ZFS. The saturation magnetization curves are again nested, but with a much larger spread than observed for the negative ZFS case. The origin of the large nesting can be seen from the energy diagram in Figure 6A. For positive ZFS, the $M_S = 0$ is lowest in energy and the ±1 is at an energy D. When the magnetic field is perpendicular to the molecular *z*-axis, the $M_S = 0$ and one component of the $M_S = \pm1$ behave very much like the ±2 non-Kramers doublet. They Zeeman split with $g \approx 8$, and the wave functions change in the same nonlinear way. However, the energy splitting at zero magnetic field is D, the axial spin Hamiltonian parameter that is much greater than δ, the rhombic splitting. Hence the saturation magnetization curves are more nested. We can now recognize a positive ZFS case from the large nesting and, using the model in Figure 6A with appropriate orientation averaging, fit the VTVH MCD data to extract spin Hamiltonian parameters, which can again be interpreted in terms of t_{2g} orbital splitting as described above.

Thus, for the complexes in Figure 2, we are now able to obtain experimentally the ligand field energies of the five d-orbitals of the ferrous site (Figure 7). We have a direct probe of geometric and electronic structure of non-heme ferrous active sites and can use this to obtain molecular-level insight into catalytic mechanisms.

Geometric and Electronic Structure/Function Correlations. We now consider the pterin-dependent non-heme iron hydroxylases as an example of the application of this VTVH MCD methodology to obtain molecular insight into catalytic mechanism.[11,12] This class includes tryptophan, tyrosine, and

---

(10) Campochiaro, C.; Pavel, E. G.; Solomon, E. I. *Inorg. Chem.* **1995**, *34*, 4669−4675.

(11) Loeb, K. E.; Westre, T. E.; Kappock, T. J.; Mitic, N.; Glasfeld, E.; Caradonna, J. P.; Hedman, B.; Hodgson, K. O.; Solomon, E. I. *J. Am. Chem. Soc.* **1997**, *119*, 1901−1915.

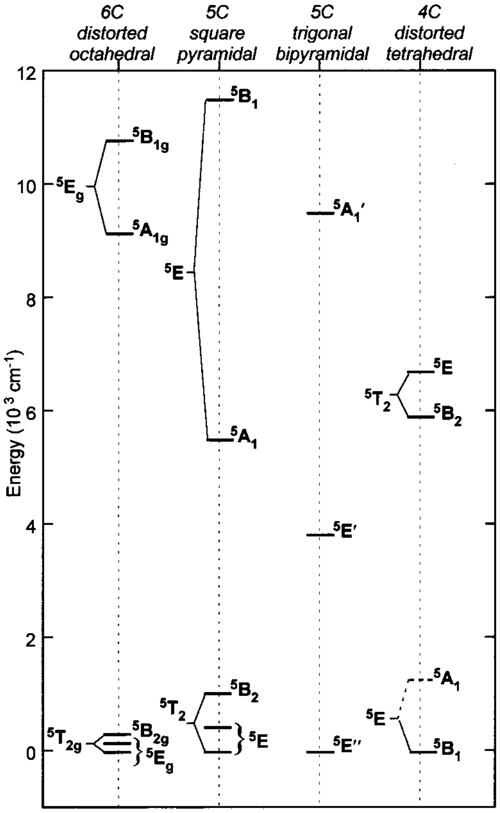

Figure 7. Experimentally determined ligand field splittings of the five d-orbitals for the complexes shown in Figure 2. (Adapted from refs 2 and 6.)

Scheme 1

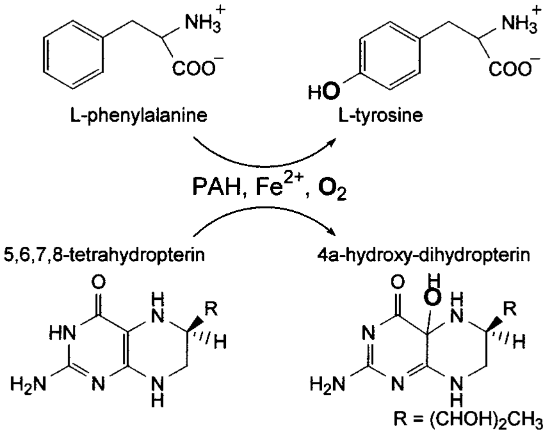

phenylalanine (PAH) hydroxylase where we focus on PAH as it is the most well-studied member of this class. It is responsible for the genetic disorder phenylketonuria (PKU), in which mutations of PAH lower its turnover, leading to a buildup of phenylalanine, resulting in severe mental retardation.[13] The reaction catalyzed by PAH is given in Scheme 1, where the high-spin ferrous active site reacts with O_2 to both hydroxylate phenylalanine to tyrosine and oxidize reduced pterin to 4a-hydroxy-dihydropterin, which then dehydrates.[14]

The black spectrum in Figure 8A presents the first insight available into the catalytically relevant ferrous active site of PAH.[11] There are two ligand field transitions in the 10000 cm^{-1} region split by less than 2000 cm^{-1}, indicating that the resting ferrous active site is 6-coordinate. Binding of the substrate phenylalanine to the active site pocket (blue spectrum in Figure 8A) shifts the ligand field transitions to slightly higher energy, indicating that substrate binds near the Fe^{II} center and perturbs the still 6-coordinate site. Binding of pterin cofactor to PAH (Figure 8B green) does not affect the Fe^{II} active site, indicating that it does not bind to the iron.[12] Importantly, when both substrate and cofactor are simultaneously bound to the enzyme, the red low-temperature MCD spectrum in Figure 8C is obtained; one transition in the 10000 cm^{-1} region and a second in the 5000 cm^{-1} region indicate that the site has become 5-coordinate. VTVH MCD data also strongly support a dramatic change in the ferrous active site. The data for the resting site (Figure 9A) show the now normal nesting (vide supra) associated with the negative ZFS splitting case, and their non-Kramers analysis gives the $^5T_{2g}$ splitting of the resting ferrous site given at the bottom left of Figure 9C. For the substrate- plus cofactor-bound site the nesting has greatly increased, indicating that the ZFS is now positive (Figure 9B). Analysis using the positive ZFS model in Figure 6A gives the $^5T_{2g}$ splitting at the bottom right of Figure 9C. From Figure 9C, when both substrate and pterin are bound to the enzyme, $10Dq$ decreases substantially and both the e_g and t_{2g} orbital splittings greatly increase. This clearly requires that the simultaneous binding of both cosubstrates to the active site leads to loss of a ligand (likely H_2O), resulting in an open coordination position for the O_2 reaction.

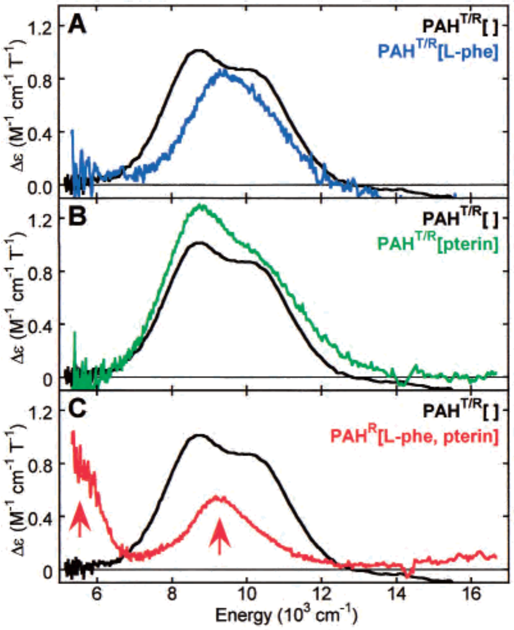

Figure 8. Low-temperature MCD spectra of PAH: PAH^{T}[ ] (black), PAH$^{T/R}$[L-Phe] (blue), PAH$^{T/R}$[pterin] (green), and PAH^{R}[L-Phe,pterin] (red). (Adapted from refs 2, 11, and 12.)

We have now observed parallel behavior over many members of the class of non-heme ferrous enzymes (pterin-[12] and α-ketoglutarate-dependent[15,16] enzymes, Rieske dioxygenases,[17]

---

(12) Kemsley, J. N.; Mitic, N.; Loeb Zaleski, K.; Caradonna, J. P.; Solomon, E. I. *J. Am. Chem. Soc.* **1999**, *121*, 1528−1536.

(13) Scriver, C. R.; Eisensmith, R. C.; Woo, S. L. C.; Kaufman, S. *Annu. Rev. Genet.* **1994**, *28*, 141−165.

(14) Lazarus, R. A.; DeBrosse, C. W.; Benkovic, S. J. *J. Am. Chem. Soc.* **1982**, *104*, 6869−6871.

(15) Zhou, J.; Gunsior, M.; Bachmann, B. O.; Townsend, C. A.; Solomon, E. I. *J. Am. Chem. Soc.* **1998**, *120*, 13539−13540.

(16) Zhou, J.; Kelly, W. L.; Bachmann, B. O.; Gunsior, M.; Townsend, C. A.; Solomon, E. I. Submitted for publication.

(17) Pavel, E. G.; Martins, L. J.; Ellis, W. R., Jr.; Solomon, E. I. *Chem. Biol.* **1994**, *1*, 173−183.

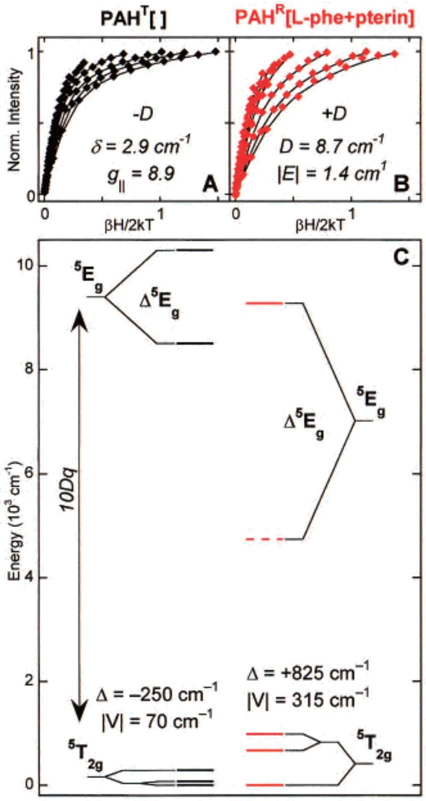

Figure 9. VTVH MCD data for PAH: (A) PAH^T[ ] and (B) PAH^R[L-Phe,pterin]. (C) Experimentally determined d-orbital energy levels for PAH^T[ ] (left) and PAH^R[L-Phe,pterin] (right). (Adapted from refs 2, 11, and 12.)

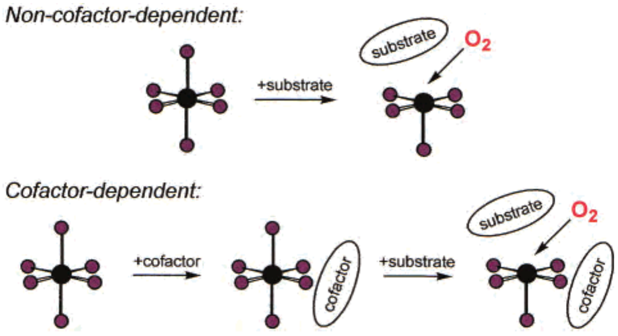

Figure 10. General mechanistic strategy for mononuclear non-heme Fe^{II} enzymes. (Adapted from ref 2.)

isopenicillin N-synthase (IPNS),[18] ethylene-forming enzyme,[19] etc.), and this has led to the general mechanistic strategy for these enzymes given in Figure 10.[12,15] The resting sites are 6-coordinate and relatively unreactive with dioxygen. Upon substrate binding to the protein for the non-cofactor-dependent enzymes or cofactor plus substrate binding for the cofactor-dependent enzymes, the iron site goes 5-coordinate. This allows the O$_2$ reaction to generate highly reactive oxygen intermediates only in the presence of substrates, leading to the direct hydroxylation of substrate or the coupled hydroxylation of cosubstrates for the cofactor-dependent non-heme iron enzymes. Thus nature has evolved an elegant mechanism to control the generation of reactive dioxygen intermediates only in the presence of substrate(s).

Oxygen Intermediates. Reaction of high-spin ferrous sites with O$_2$ leads to the generation of oxygen intermediates that catalyze the organic transformations in Table 1. Thus far only in the case of bleomycin has this intermediate been stabilized allowing detailed spectroscopic and electronic structure study. Ferrous bleomycin reacts with O$_2$ and a second exogenous electron to generate activated bleomycin, the species that is kinetically competent to cleave DNA by H-atom abstraction.[20] A variety of studies have led to its description as a low-spin ferric–hydroperoxide complex.[21–23] We have now obtained detailed spectroscopic data on activated bleomycin and used these data to evaluate and calibrate electronic structure calculations.[24] These give the optimized geometric structure of activated bleomycin on the left in Figure 11A. The hydroperoxide binds with an Fe–O–O angle of ~120°, bisecting the two chemically interesting ligands, namely, the deprotonated amide and the pyrimidine nitrogen.

These experimentally supported calculations allow for evaluation of the heterolytic O–O bond cleavage reaction coordinate generally considered to be relevant in heme chemistry.[24] From the right side of Figure 11A, as found in heme chemistry, heterolytic cleavage of the peroxide bond in activated bleomycin produces a ferryl species (Fe^{IV}=O) with concomitant oxidation of the deprotonated amide ligand. From the energetics of the potential energy surfaces in Figure 11B, in contrast to heme systems where heterolytic cleavage is highly exothermic, this reaction is energetically unfavorable for bleomycin and even more so for non-heme iron sites with more innocent ligand sets. This is because ligand oxidation in P450 is much more stabilized by delocalization of the hole produced over the porphyrin ligand and by the large anionic charge donation. This is observed experimentally from the ligand-to-Fe^{III} charge-transfer energies for bleomycin relative to heme systems, where the charge-transfer transitions can be identified by low-temperature MCD spectroscopy. From Figure 11C the ligand-to-metal charge-transfer transition of the deprotonated amide is almost 2.5 eV higher in energy than the porphyrin charge transfer (both to low-spin ferric centers). Thus non-heme ligand oxidation is thermodynamically unfavorable (even for the deprotonated amide), and an alternative mechanism for oxygen activation is likely operative for mononuclear non-heme iron sites.

An alternative hypothesis is direct H-atom abstraction from substrate by the hydroperoxide–Fe^{III} bleomycin complex (Figure 11D). As schematically illustrated in Figure 11E, *protonation of the peroxide greatly lowers the energy of its* σ^* *orbital*, activating the peroxide for electrophilic attack on substrate. This would shift electron density out of the H–C σ bond and into the σ^* orbital of peroxide, which would weaken both bonds and promote H-atom transfer to the peroxide. The driving force for this reaction is the formation of water and the Fe^{IV}=O species, which is stabilized by both strong σ- and π-donor bonds.

Binuclear Non-Heme Iron Proteins

Table 2 gives a partial list of the binuclear non-heme iron proteins under investigation in our labs. The first four are

---

(18) Roach, P. L.; Clifton, I. J.; Hensgens, C. M. H.; Shibata, N.; Schofield, C. J.; Hajdu, J.; Baldwin, J. E. *Nature* **1997**, *387*, 827–830.

(19) Zhou, J.; Rocklin, A.; Lipscomb, J.; Que, L., Jr.; Solomon, E. I. Manuscript in preparation.

(20) Burger, R. M.; Peisach, J.; Horwitz, S. B. *J. Biol. Chem.* **1981**, *256*, 11636–11644.

(21) Sam, J. W.; Tang, X.-J.; Peisach, J. *J. Am. Chem. Soc.* **1994**, *116*, 5250–5256.

(22) Veselov, A.; Sun, H.; Sienkiewicz, A.; Taylor, H.; Burger, R. M.; Scholes, C. P. *J. Am. Chem. Soc.* **1995**, *117*, 7508–7512.

(23) Westre, T. E.; Loeb, K. E.; Zaleski, J. M.; Hedman, B.; Hodgson, K. O.; Solomon, E. I. *J. Am. Chem. Soc.* **1995**, *117*, 1309–1313.

(24) Neese, F.; Zaleski, J. M.; Loeb Zaleski, K.; Solomon, E. I. *J. Am. Chem. Soc.* **2000**, *122*, 11703–11724.

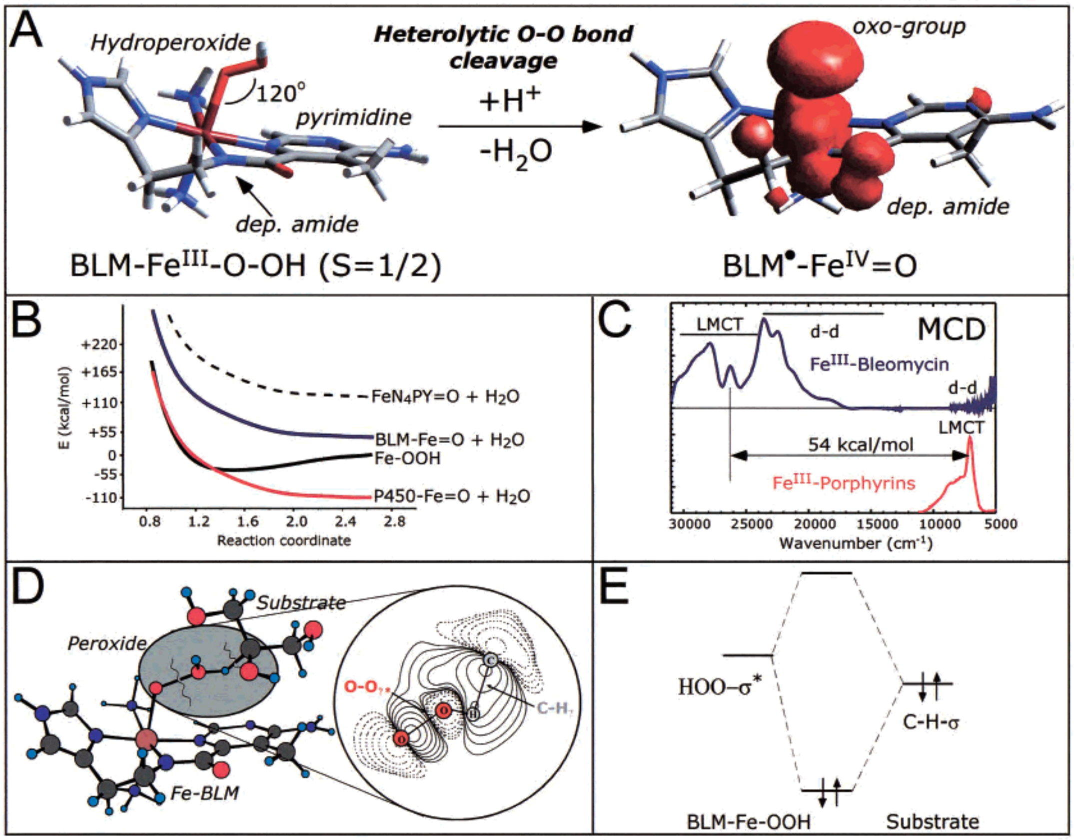

Figure 11. Electronic structure of activated bleomycin. (A) Geometry-optimized structure and effect of heterolytic cleavage of O−O bond. (B) Potential energy surfaces of activated bleomycin (blue), relative to its heterolytic cleavage, and the equivalent for the heme site in cytochrome P450 (red) and an innocent non-heme environment (dashed). (C) MCD-derived deprotonated amide-to-Fe^{III} charge transfer in bleomycin (top) and porphyrin-to-Fe^{III} charge transfer in low-spin heme (bottom). (D) Interaction of HOO−Fe^{III} bleomycin complex with substrate. (E) Schematic frontier molecular orbital description of the electrophilic attack of hydroperoxide on deoxyribose C4′−H bond. (Adapted from refs 2 and 24.)

Table 2. Binuclear Non-Heme Iron Enzymes

Reaction Type	Representative Enzyme	Catalytic Reaction		
reversible dioxygen binding	hemerythrin (Hr)	$[Fe^{II}Fe^{II}]$	$\overset{+O_2}{\rightleftharpoons}$	$[Fe^{III}Fe^{III}]$–OOH
one e$^-$ oxidation	ribonucleotide diphosphate reductase (RR)	$[Fe^{II}Fe^{II}]$ + Tyr	$\xrightarrow{+O_2}$	$[Fe^{III}Fe^{III}]$ + Tyr•
hydroxylation	methane monooxygenase (MMO)	$[Fe^{II}Fe^{II}]$ + CH_4	$\xrightarrow{+O_2}$	$[Fe^{III}Fe^{III}]$ + CH_3OH/H_2O
desaturation	stearoyl-acyl carrier protein Δ^9-desaturase (ACP Δ^9D)	$[Fe^{II}Fe^{II}]$ + Stearoyl ACP	$\xrightarrow{+O_2}$	$[Fe^{III}Fe^{III}]$ + Oleoyl ACP
hydrolysis of phosphate ester	purple acid phosphatase (PAP)	$[Fe^{II}Fe^{III}]$ + $ROHPO_3^-$	$\xrightarrow{+H_2O}$	$[Fe^{II}Fe^{III}]$ + $H_2PO_4^-$
NADH peroxidation	Rebrerythrin (Rb)	$[Fe^{II}Fe^{II}]$ + H_2O_2	$\xrightarrow{+O_2}$	$[Fe^{III}Fe^{III})]$
Ferroxidation	Ferritin	$[Fe^{II}Fe^{II}]$	$\xrightarrow{+O_2}$	$[Fe^{III}Fe^{III})]$

involved in dioxygen binding and activation using a binuclear high spin ferrous active site and are considered here. Deoxyhemerythrin reversibly binds O_2 to generate oxyhemerythrin. Ribonucleotide reductase (RR), methane monooxygenase (MMO), and Δ^9-desaturase (Δ^9D) activate dioxygen to generate a catalytically active tyrosine radical (in RR), hydroxylate methane to methanol (MMO), or generate a carbon−carbon double bond in stearoyl-bound acyl carrier protein (Δ^9D). Presented below are our earlier data on deoxyhemerythrin, which are used to develop the new spectroscopic features associated with the

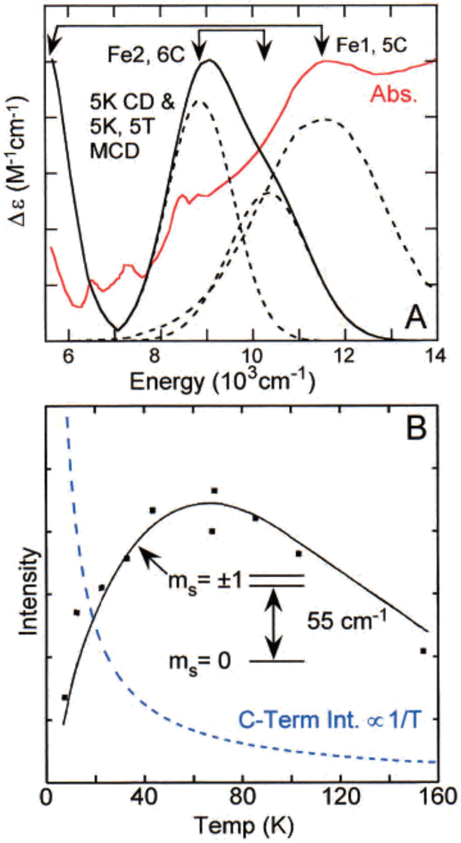

Figure 12. (A) Absorption (red), CD and low-temperature MCD (black) ligand field spectra of deoxyhemerythrin. (B) Temperature-dependent MCD intensity for deoxyhemerythrin at fixed magnetic field (black). The inset spin ladder is derived from these data, while the dashed blue line is the VT MCD behavior of an Fe^{II} monomer. (Adapted from ref 2.)

presence of a binuclear ferrous active site. This methodology is then extended over the O_2-activating enzymes RR, MMO, and Δ^9D to define structure/function correlations. In each case we consider the electronic structure of the $Fe^{III}_2(O_2^{2-})$ intermediates generated and define its contribution to the reversible binding and activation of dioxygen.

Binuclear Methodology. Figure 12A presents the low-temperature near-IR absorption, CD, and MCD spectra of deoxyhemerythrin.[25,26] Four bands are clearly observed, indicating that there are contributions from two inequivalent ferrous centers. There is one transition in the ~5000 cm $^{-1}$ region and there are three in the ~10000 cm $^{-1}$ region, indicating one 5- and one 6-coordinate iron. Thus one iron center has an open coordinate position for the O_2 reaction. When the magnetic field is turned on at low temperature, there is no change in the CD spectrum. This shows that there is no MCD signal present at low temperature. For mononuclear Fe^{II} sites, the MCD signal increases with decreasing temperature (as $1/T$, shown by the dashed line in Figure 12B). This is the *C*-term MCD behavior of paramagnetic sites. Thus the ground state of deoxyhemerythrin must be diamagnetic. As shown by the data points in Figure 12B, when the temperature is increased the MCD intensity increases, peaking at ~60 K, and then decreases with increasing temperature. This shows that there is a low-lying paramagnetic excited state that is Boltzmann populated. From a fit to the data (solid line) the energy of this state is ~55 cm^{-1} (energy level inset in Figure 12B).

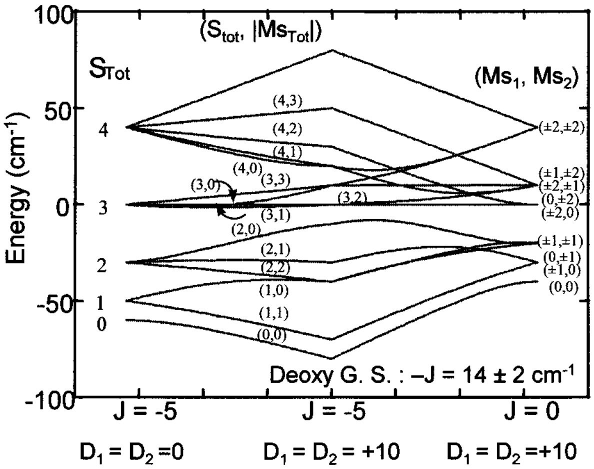

Figure 13. *J/D* diagram for deoxyhemerythrin. Left side is exchange coupling to form S_{tot} states of dimer. Right side is positive ZFS for Fe_1 and Fe_2. Center includes both terms. (Adapted from ref 25.)

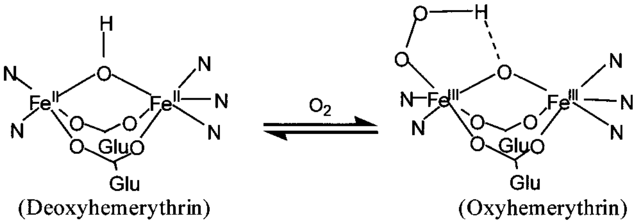

Figure 14. Reversible dioxygen binding by hemerythrin. (Adapted from ref 2.)

In Figure 13, derived from eq 2, we consider the ground-state properties of binuclear ferrous sites.[25] First, each Fe^{II} can

$$\mathcal{H} = D_1(S_{z1}^{\;2} - {}^1/_3S(S+1)) + E_1(S_{x1}^{\;2} - S_{y1}^{\;2}) + D_2(S_{z2}^{\;2} - {}^1/_3S(S+1)) + E_2(S_{x2}^{\;2} - S_{y2}^{\;2}) - 2J\mathbf{S}_1\cdot\mathbf{S}_2 \quad (2)$$

undergo ZFS, and if both are positive the energy diagram on the right is obtained. The $M_S = 0$ is lowest in energy for each iron and the $M_S = \pm1$ is D cm^{-1} higher in energy. This would fit the data points in Figure 12 (with the $M_S = 0$ ground-state diamagnetic and the ±1 the paramagnetic excited state) with an energy D of ~35 cm $^{-1}$. However, the highest experimentally observed or theoretically predicted D value for high-spin ferrous centers is about 15 cm^{-1}. Therefore, there must be an additional interaction present in the binuclear ferrous active site of deoxyhemerythrin. This is the exchange coupling of the two $S = 2$ ions through a bridging ligand, which is given by the Heisenberg, Dirac, Van Vleck Hamiltonian, $-2J\mathbf{S}_1\cdot\mathbf{S}_2$. This term couples the two $S = 2$ to form total spin states of the binuclear ferrous site: $S_{tot} = |S_1 + S_2| \ldots |S_1 - S_2| = 4, 3, 2, 1, 0$. For antiferromagnetic coupling the $S_{tot} = 0$ is lowest in energy with the $S_{tot} = 1$ at an excited-state energy of $2J$ (left limit of Figure 13). This fits the VT MCD data in Figure 12 with an antiferromagnetic coupling $-J$ of 25 cm^{-1}. For binuclear ferrous systems, however, this value of the exchange is comparable to the ZFS and one must simultaneously solve the complete Hamiltonian in eq 2, which gives the center portion of the *J/D* diagram in Figure 13. Application of this complete Hamiltonian to the spectroscopic and magnetic data for deoxyhemerythrin

---

(25) Reem, R. C.; Solomon, E. I. *J. Am. Chem. Soc.* **1987**, *109*, 1216–1226.

(26) Reem, R. C.; Solomon, E. I. *J. Am. Chem. Soc.* **1984**, *106*, 8323–8325.

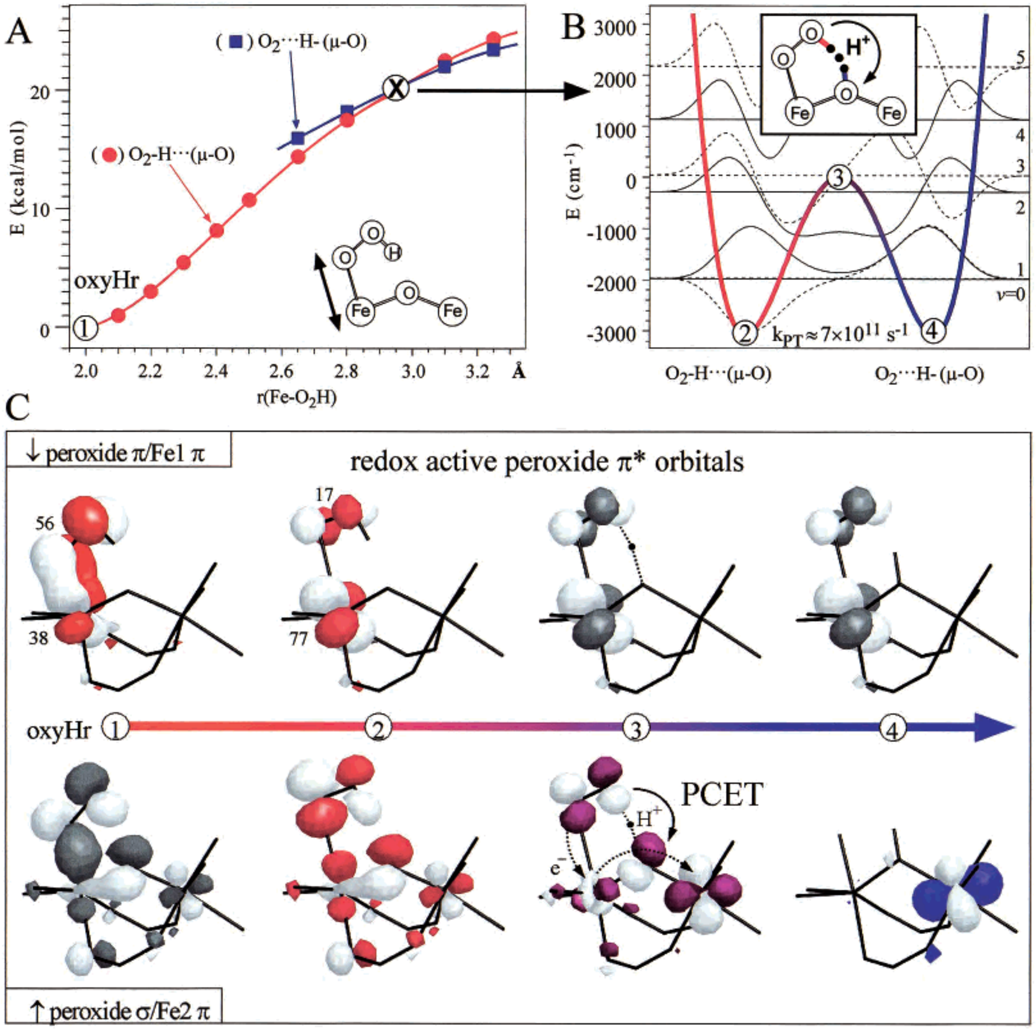

Figure 15. (A) DFT calculated potential energy surface for elongation of the Fe−(O_2H) bond in oxyhemerythrin (red) and elongation of the Fe−(O_2) bond with the proton transferred to the oxo bridge (blue). (B) Proton tunneling at an Fe−(O_2H) bond length of 2.95 Å in oxyhemerythrin. The potential energy barrier is modeled as a quadratic function. (C) Redox active orbital changes in the peroxide π-bonding and σ-bonding orbitals over the reaction coordinates of Fe−(O_2H) bond elongation and proton transfer. (Adapted from ref 2.)

gives an antiferromagnetic coupling $-J$ of 14 ± 2 cm^{-1}.[25,27] This is large for a binuclear ferrous site and first indicated the presence of a hydroxide bridge,[26] which was subsequently supported by model studies[28] and crystallography.[29]

Thus deoxyhemerythrin has one 5-and one 6-coordinate Fe^{II} center bridged by OH^- (Figure 14 left). O_2 reacts at the open coordination position of the 5-coordinate center to generate oxyhemerythrin, which is known from spectroscopy and crystallography to be a hydroperoxide bound to one iron of an oxo-bridged ferric dimer (Figure 14, right). This reaction involves the transfer of two electrons and a proton to O_2 binding at a single iron site.

Reversible O_2 Binding: Proton-Coupled Electron Transfer. The spectroscopic and magnetic data on deoxyhemerythrin and a larger body of data on oxyhemerythrin have been used to evaluate electronic structure calculations. Experimentally supported calculations then allow one to interpolate between structures and generate an electronic structure description for the reversible binding of dioxygen by hemerythrin.[27,30] Figure 15A gives the change in total energy and Figure 15C the change in the two redox active π* orbitals of peroxide as the Fe−(O_2H) bond is elongated along the reaction coordinate associated with the reversible loss of O_2. From Figure 15C (top), charge initially transfers from the peroxide π* orbital into the d_π orbital of the coordinated iron (geometries 1 and 2). Associated with this, the energy of the complex increases as the charge transfer raises the pK_a of the oxo bridge and lowers that of the hydroperoxide. At an Fe−(O_2H) distance of ~2.95 Å it becomes isoenergetic to have the proton on either the peroxide or the oxo bridge. This is a double minimal problem, and we have solved this (Figure 15B) to estimate the rate of proton tunneling through the barrier. This tunneling is fast, consistent with the low kinetic isotope effect observed[31] in reversible O_2 binding. As the proton is transferred from the peroxide to the oxo bridge, the second electron is transferred from the peroxide π* orbital that is σ-bonding to the coordinated iron to the d_π orbital of the other iron (Figure 15C, bottom, geometries 2, 3, and 4). This describes a proton-coupled electron transfer (PCET). However, it is not a hydrogen atom transfer as can be seen from the transition

---

(27) Brunold, T. C.; Solomon, E. I. *J. Am. Chem. Soc.* **1999**, *121*, 8277−8287.

(28) Chaudhuri, P.; Wieghardt, K.; Nuber, B.; Weiss, J. *Angew. Chem., Int. Ed. Eng.* **1985**, *24*, 778−779.

(29) Stenkamp, R. E. *Chem. Rev.* **1994**, *94*, 715−726.

(30) Brunold, T. C.; Solomon, E. I. *J. Am. Chem. Soc.* **1999**, *121*, 8288−8295.

(31) Armstrong, G. D.; Sykes, A. G. *Inorg. Chem.* **1986**, *25*, 3135−3139.

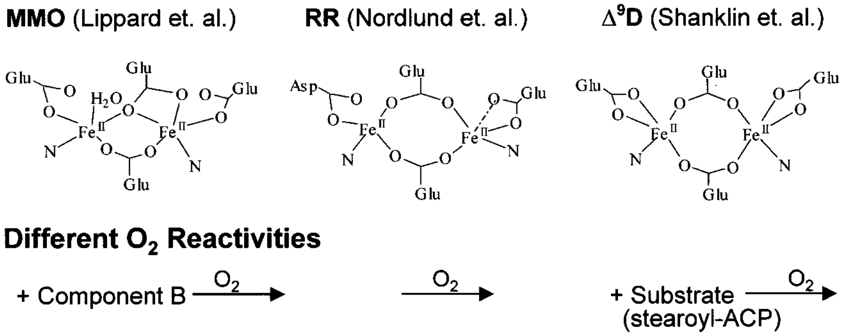

Figure 16. Comparison of MMO/RR/Δ^9D reduced structures and their relation to reactivity. Note: Spectroscopic data on reduced RR indicate that one iron is 5-coordinate. (Adapted from ref 2.)

state for the proton transfer (Figure 15C, bottom, geometry 3). The electron transfer takes a different path from the proton, through the oxo bridge. Very importantly, this involves the σ/π pathway of the oxo bridge, which is the same pathway that we[32,33] and others[34,35] have shown plays the major role in antiferromagnetic coupling in bent ferric−oxo dimers. Thus this study allows one to correlate antiferromagnetic coupling in homodimers with superexchange pathways for electron transfer. A quantitative description of this is given in ref 36.

O$_2$ Activation: Structure/Function Correlations. While MMO, RR, and Δ^9D catalyze different reactions (Table 2), these seem to involve similar dioxygen intermediates, in particular a peroxide intermediate P[37−42] that goes on to generate high-valent iron−oxo intermediates (Q in MMO,[43,44] X in RR[45−48]). The nature of P and its activation to form high-valent intermediates is considered in the next section. Here we focus on the fact that these similar intermediates are generated by resting reduced active sites that have different structures (Figure 16). MMO has two 5-coordinate irons bridged by μ-1,1- and μ-1,3-carboxylates.[49] RR has one 4- and one 5-coordinate iron bridged by two μ-1,3-carboxylates. While crystallography for RR indicates two 4-coordinate Fe$^{\mathrm{II}}$ centers,[50] CD/MCD in solution indicate that one Fe$^{\mathrm{II}}$ is 5-coordinate.[51] Δ^9D has two 5-coordinate irons with two μ-1,3-carboxylate bridges.[52] Importantly, only resting reduced RR rapidly reacts with dioxygen. For MMO, a coupling protein (component B) is required for the rapid reaction with O$_2$,[53,54] and in Δ^9D the substrate (stearoyl−acyl carrier protein) needs to be bound to the enzyme for the O$_2$ reaction.[55] While the spectroscopic/structural changes associated with component B binding to reduced MMO still need to be defined, substrate binding to Δ^9D has been studied in detail.

Figure 17A gives the near-IR CD/MCD spectra of resting reduced Δ^9D.[56] Two ligand field transitions are observed, one in the low-energy region and the second in the high-energy region, indicating that this site has two equivalent 5-coordinate irons, consistent with the crystal structure on the right in Figure 16. Note that the excited-state splitting is ∼3000 cm^{-1} rather than the ∼5000 cm^{-1} generally observed for square pyramidal Fe$^{\mathrm{II}}$ centers. Ligand field calculations show that this decreased splitting derives from the bidentate carboxylate present at each iron center. These carboxylates have a bite angle of ∼55° that produces an in/out distortion in the equatorial plane. In contrast to deoxyhemerythrin, reduced Δ^9D has a large low-temperature MCD signal, indicating that the antiferromagnetic coupling is greatly reduced. A fit to the VTVH MCD data in Figure 17B gives weak antiferromagnetic coupling ($J \approx -0.5$ cm^{-1}), consistent with the μ-1,3-carboxylate bridges in Figure 16 and a negative ZFS as expected for square pyramidal ferrous centers. Upon binding substrate these spectra dramatically change. From Figure 17C the near-IR CD/MCD spectra now show three bands, one at high energy and two in the low-energy region, indicating that there is now one 5- and one 4-coordinate Fe$^{\mathrm{II}}$ center. The VTVH MCD data (Figure 17D) again show a paramagnetic ground state indicating weak antiferromagnetic coupling. However, there is now an inverse saturation behavior, which indicates

---

(32) Reem, R. C.; McCormick, J. M.; Richardson, D. E.; Devlin, F. J.; Stephens, P. J.; Musselman, R. L.; Solomon, E. I. *J. Am. Chem. Soc.* **1989**, *111*, 4688−4704.

(33) Brown, C. A.; Remar, G. J.; Musselman, R. L.; Solomon, E. I. *Inorg. Chem.* **1995**, *34*, 688−717.

(34) Bossek, U.; Weyermüller, T.; Wieghardt, K.; Bonvoisin, J.; Girerd, J.-J. *J. Chem. Soc., Chem. Commun.* **1989**, 633−636.

(35) Hotzelmann, R.; Wieghardt, K.; Flörke, U.; Haupt, H.-J.; Weatherburn, D. C.; Bonvoisin, J.; Blondin, G.; Girerd, J.-J. *J. Am. Chem. Soc.* **1992**, *114*, 1681−1696.

(36) Brunold, T. C.; Gamelin, D. R.; Solomon, E. I. *J. Am. Chem. Soc.* **2000**, *122*, 8511−8523.

(37) Andersson, K. K.; Froland, W. A.; Lee, S.-K.; Lipscomb, J. D. *New J. Chem.* **1991**, *15*, 411−415.

(38) Liu, K. E.; Valentine, A. M.; Qiu, D.; Edmondson, D. E.; Appelman, E. H.; Spiro, T. G.; Lippard, S. J. *J. Am. Chem. Soc.* **1995**, *117*, 4997−4998.

(39) Kim, K.; Lippard, S. J. *J. Am. Chem. Soc.* **1996**, *118*, 4914−4915.

(40) Liu, K. E.; Valentine, A. M.; Qiu, D.; Edmondson, D. E.; Appelman, E. H.; Spiro, T. G.; Lippard, S. J. *J. Am. Chem. Soc.* **1997**, *119*, 11134−11135.

(41) Bollinger, J. M., Jr.; Krebs, C.; Vicol, A.; Chen, S.; Ley, B. A.; Edmondson, D. E.; Huynh, B. H. *J. Am. Chem. Soc.* **1998**, *120*, 1094−1095.

(42) Broadwater, J. A.; Achim, C.; Münck, E.; Fox, B. G. *Biochemistry* **1999**, *38*, 12197−12204.

(43) Lee, S.-K.; Fox, B. G.; Froland, W. A.; Lipscomb, J. D.; Munck, E. *J. Am. Chem. Soc.* **1993**, *115*, 6450−6451.

(44) Lee, S.-K.; Nesheim, J. C.; Lipscomb, J. D. *J. Biol. Chem.* **1993**, *268*, 21569−21577.

(45) Bollinger, J. M., Jr.; Tong, W. H.; Ravi, N.; Huynh, B. H.; Edmondson, D. E.; Stubbe, J. *J. Am. Chem. Soc.* **1994**, *116*, 8015−8023.

(46) Bollinger, J. M., Jr.; Tong, W. H.; Ravi, N.; Huynh, B. H.; Edmondson, D. E.; Stubbe, J. *J. Am. Chem. Soc.* **1994**, *116*, 8024−8032.

(47) Ravi, N.; Bollinger, J. M., Jr.; Huynh, B. H.; Edmondson, D. E.; Stubbe, J. *J. Am. Chem. Soc.* **1994**, *116*, 8007−8014.

(48) Tong, W. H.; Chen, S.; Lloyd, S.; Edmondson, D.; Huynh, B. H.; Stubbe, J. *J. Am. Chem. Soc.* **1996**, *118*, 2107−2108.

(49) Rosenzweig, A. C.; Nordlund, P.; Takahara, P. M.; Frederick, C. A.; Lippard, S. J. *Chem. Biol.* **1995**, *2*, 409−418.

(50) Nordlund, P.; Sjöberg, B.-M.; Eklund, H. *Nature* **1990**, *345*, 593−598.

(51) Pulver, S. C.; Tong, W. H.; Bollinger, J. M., Jr.; Stubbe, J.; Solomon, E. I. *J. Am. Chem. Soc.* **1995**, *117*, 12664−12678.

(52) Lindqvist, Y.; Huang, W.; Schneider, G.; Shanklin, J. *EMBO J.* **1996**, *15*, 4081−4092.

(53) Fox, B. G.; Liu, Y.; Dege, J. E.; Lipscomb, J. D. *J. Biol. Chem.* **1991**, *266*, 540−550.

(54) Liu, K. E.; Valentine, A. M.; Wang, D. L.; Huynh, B. H.; Edmondson, D. E.; Salifoglou, A.; Lippard, S. J. *J. Am. Chem. Soc.* **1995**, *117*, 10174−10185.

(55) Broadwater, J. A.; Ai, J. Y.; Loehr, T. M.; Sanders-Loehr, J.; Fox, B. G. *Biochemistry* **1998**, *37*, 14664−14671.

(56) Yang, Y.-S.; Broadwater, A.; Fox, B. G.; Solomon, E. I. *J. Am. Chem. Soc.* **1999**, *121*, 2770−2787.

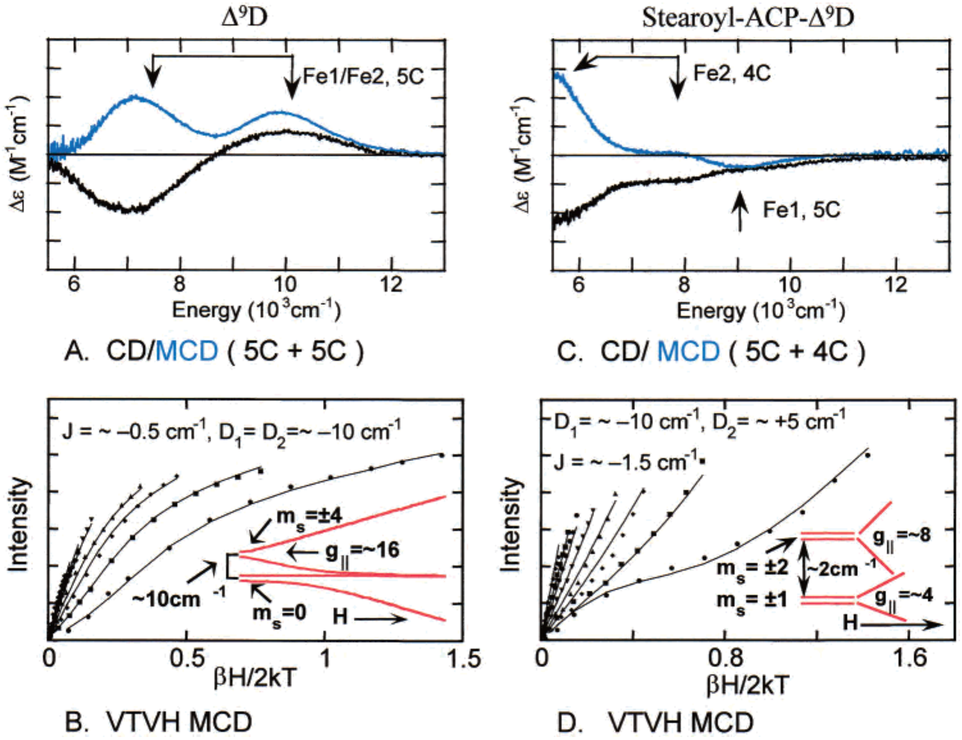

Figure 17. CD/MCD spectra for reduced Δ^9D (A) and stearoyl-ACP-Δ^9D (C). For the VTVH MCD data in B and D, the derived energy levels in a magnetic field are included as well as the J and D values. (Adapted from ref 2.)

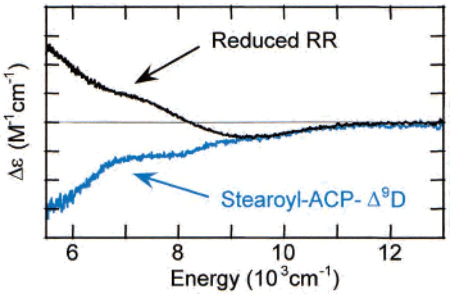

Figure 18. Near-IR CD comparison of stearoyl-ACP-Δ^9D to reduced RR. (Adapted from ref 2.)

Table 3. Ground-State Parameters (from VTVH MCD)

	stearoyl-ACP Δ^9-desaturase	reduced RR
J (cm$^{-1)}$	-1.5	-0.5
D_1 (cm^{-1})	~ -10	~ -10
D_2 (cm^{-1})	$\sim +5$	$\sim +5$

that an excited state crosses over to become the ground state at high magnetic field. This requires that the ZFS of one Fe^{II} center has become positive, consistent with the presence of a distorted 4-coordinate Fe^{II} center in the structure of substrate-bound Δ^9D.

Figure 18 compares the spectrum of substrate-bound Δ^9D to that of resting reduced RR. Both show three ligand field transitions at similar energies, and from Table 3 similar weak antiferromagnetic coupling and one positive and one negative ZFS. Thus, upon substrate binding the active site of Δ^9D becomes very similar to that of resting reduced RR.

These results lead to a general mechanistic strategy for binuclear non-heme iron enzymes (Figure 19) that is very similar to that of the mononuclear non-heme iron sites in Figure 10.[57] The resting site of Δ^9D is unreactive with O_2; however, substrate binding opens an additional coordination position at the iron allowing the O_2 reaction only in the presence of substrate. Further, substrate binding changes the Δ^9D active site structure to become very similar to that of resting reduced RR. This site structure can rapidly react with O_2 as the substrate is a tyrosine residue that is already present at the active site. Thus, at least for these binuclear non-heme iron enzymes, there appears to be a common reactive site structure involved in dioxygen activation to generate intermediate P.

Oxygen Intermediates. As emphasized in Figure 20, the binuclear ferrous sites of MMO, RR, and Δ^9D react with dioxygen to generate similar peroxide intermediates P,[41] which further convert to high-valent iron−oxo intermediates, Q (MMO) and X (RR). We now consider the geometric and electronic structure of P and its activation to generate high-valent intermediates, and how this relates to the mononuclear non-heme iron chemistry considered in the first part of this presentation.

While limited data are available on P in MMO, the peroxy intermediates of Δ^9D[55] and mutant forms of RR can be stabilized for spectroscopy. The peroxide intermediate of RR[58] exhibits unusual spectroscopic features (Figure 21) that include a high-frequency $\nu_{\mathrm{o-o}}$,[59] which profiles the peroxide-to-Fe^{III} charge-transfer transitions such that the resonance enhancement from the π charge transfer is strong while that from the σ charge transfer is weak.[60] This is the same spectroscopic behavior observed for structurally defined *cis*-μ-1,2-peroxy bridged

---

(57) Yang, Y.-S.; Baldwin, J.; Ley, B. A.; Bollinger, J. M., Jr.; Solomon, E. I. *J. Am. Chem. Soc.* **2000**, *122*, 8495−8510.

(58) Bollinger, J. M., Jr.; Krebs, C.; Vicol, A.; Chen, S.; Ley, B. A.; Edmondson, D. E.; Huynh, B. H. *J. Am. Chem. Soc.* **1998**, *120*, 1094−1095.

(59) Moënne-Loccoz, P.; Krebs, C.; Herlihy, K.; Edmondson, D. E.; Theil, E. C.; Huynh, B. H.; Loehr, T. M. *Biochemistry* **1999**, *38*, 5290−5295.

(60) Brunold, T. C.; Skulan, A. J.; Lyle, K. S.; Baldwin, J.; Fox, B. G.; Bollinger, J. M., Jr.; Solomon, E. I. Manuscript in preparation.

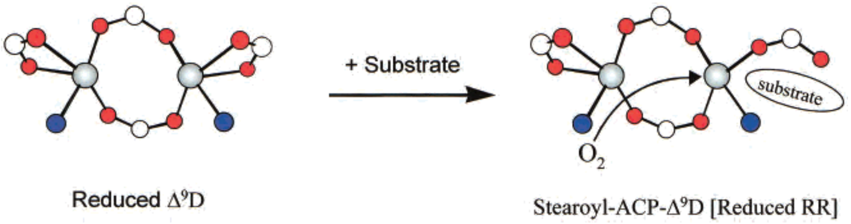

Figure 19. General mechanistic strategy for binuclear non-heme iron enzymes. (Adapted from ref 2.)

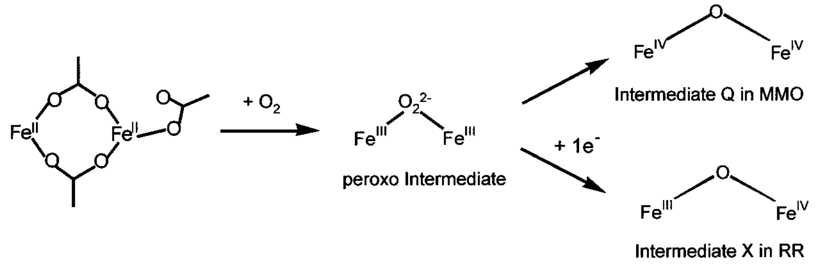

Figure 20. Reaction of active binuclear ferrous sites with dioxygen to give peroxy intermediate and then high-valent μ-oxo intermediates. (Adapted from ref 41.)

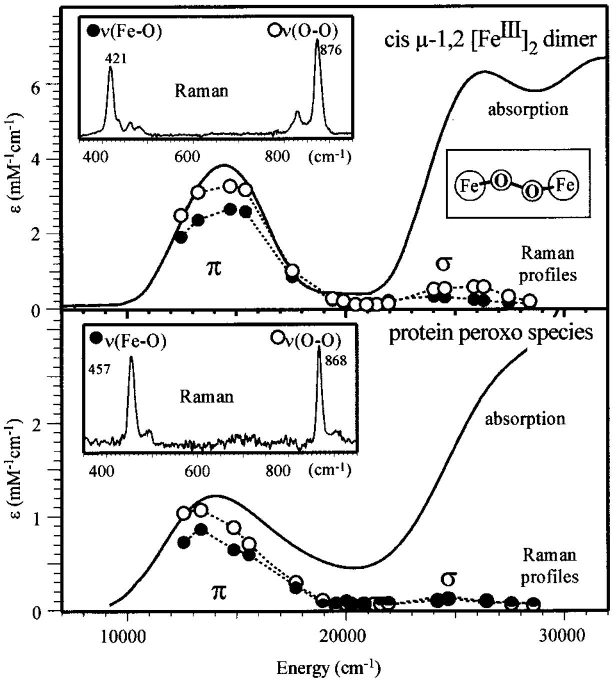

Figure 21. Comparison of *cis*-μ-1,2 peroxo Fe^{III}_2 model complex absorption spectrum and rR profiles (top) with those of the peroxo intermediate of the D84E mutant of ribonucleotide reductase (bottom). Relevant rR spectra are given in both panels. (Adapted from ref 2.)

binuclear ferric model complexes;[61] thus the peroxy intermediate in RR has a similar geometric and electronic structure.

The electronic structure can be experimentally and theoretically studied in more detail in the model complex. The high value of ν_{O-O} which results from a large Fe−O−O angle and the dominantly π rR enhancement reflect a large π contribution to the limited peroxide-to-iron charge donation. This results in a relatively basic peroxide that is activated for nucleophilic attack.[61] Thus a reasonable mechanism for the conversion of P to Q is protonation of the peroxide to form a μ-1,1-hydroperoxide structure (Figure 22, top).[2,60] As emphasized for the oxygen intermediates in the mononuclear non-heme iron sites, protonation of peroxide stabilizes the energy of its σ^* orbital, which activates it for the two-electron reductive cleavage of the O−O bond. This will generate a high-valent μ-oxo−Fe^{IV}_2 intermediate where the driving force for this reaction is the formation of water and the oxo bridge. Importantly, this chemistry differs from that of mononuclear non-heme iron in that the second iron provides the second electron and oxidation of Fe^{III} to the ferryl level is easier than oxidation of a non-heme ligand. It should be noted that the alternative mechanism often invoked is the side-on to bis-μ-oxo rearrangement (Figure 22, bottom) observed in Cu_2O_2 chemistry.[62] We do not favor this reaction as it involves rearrangement of a π-bonded, end-on bridged peroxide intermediate to a σ-bonded side-on peroxide. Also, peroxide side-on bound to Fe^{III} does not show π-back-bonding into the peroxide σ^* orbital[63] that is present in the μ-η^2:η^2-O_2^{2-}−Cu^{II}_2 system[64,65] and lowers the activation barrier for its conversion to the bis μ-oxo-Cu^{III}_2 structure.[66] ($\nu_{O-O}(\eta^2\text{-Fe}^{III})$ = 816 cm^{-1},[63,67] while $\nu_{O-O}(\mu\text{-}\eta^2\text{:}\eta^2\text{-O}_2^{2-}\text{−Cu}^{II}_2)$ = 750 cm^{-1},[68] where the low frequency of the latter reflects the π-back-bonding.)[64,65] Further insight into this reaction coordinate and evaluation of the possibilities in Figure 22 requires detailed spectroscopic characterization of Q and X. Importantly, both possible reaction coordinates involve the two-electron reductive cleavage of the peroxide O−O bond by oxidation of two Fe^{III} to generate a μ-oxo−Fe^{IV}_2 reactive species. Several Fe^{IV}−oxo species now exist,[69,70] and their spectroscopic characterization will experimentally define their electronic

---

(61) Brunold, T. C.; Tamura, N.; N., K.; MoroOka, Y.; Solomon, E. I. *J. Am. Chem. Soc.* **1998**, *120*, 5674−5690.

(62) Halfen, J. A.; Mahapatra, S.; Wilkinson, E. C.; Kaderli, S.; Young, V. G., Jr.; Que, L., Jr.; Zuberbühler, A. D.; Tolman, W. B. *Science* **1996**, *271*, 1397−1400.

(63) Neese, F.; Solomon, E. I. *J. Am. Chem. Soc.* **1998**, *120*, 12829−12848.

(64) Ross, P. K.; Solomon, E. I. *J. Am. Chem. Soc.* **1990**, *112*, 5871−5872.

(65) Ross, P. K.; Solomon, E. I. *J. Am. Chem. Soc.* **1991**, *113*, 3246−3259.

(66) Henson, M. J.; Mukherjee, P.; Root, D. E.; Stack, T. D. P.; Solomon, E. I. *J. Am. Chem. Soc.* **1999**, *121*, 10332−10345.

(67) Ahmad, S.; McCallum, J. D.; Shiemke, A. K.; Appelman, E. H.; Loehr, T. M.; Sanders-Loehr, J. *Inorg. Chem.* **1988**, *27*, 2230−2233.

(68) Baldwin, M. J.; Root, D. E.; Pate, J. E.; Fujisawa, K.; Kitajima, N.; Solomon, E. I. *J. Am. Chem. Soc.* **1992**, *114*, 10421−10431.

(69) Wilkinson, E. C.; Dong, Y. H.; Y., Z.; Fujii, H.; Fraczkiewicz, R.; Fraczkiewicz, G.; Czernuszewicz, R. S.; Que, L. *J. Am. Chem. Soc.* **1998**, *120*, 955−962.

(70) Mukerjee, S.; Stassinopoulos, A.; Caradonna, J. P. *J. Am. Chem. Soc.* **1997**, *119*, 8097−8098.

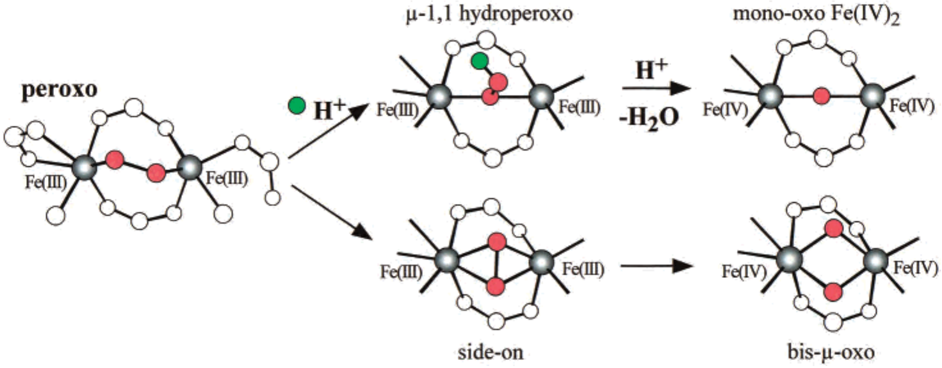

Figure 22. Two possible reaction pathways for dioxygen bond cleavage and formation of a high-valent iron−oxo intermediate. Top: protonation and heterolytic cleavage of O−O bond. Bottom: end-on to side-on rearrangement with homolytic cleavage of O−O bond.

structure and this contribution to reactivity.

Concluding Comments

While it has taken a concerted effort over a number of years to develop a new spectroscopic approach to study non-heme iron centers, the rewards have been exciting in that we can now look at reaction mechanisms experimentally on a molecular level. This has led to a general mechanistic strategy utilized by many enzymes in this class that allows the generation of reactive oxygen intermediates only in the presence of substrates. Further, the electronic structure of these intermediates is fundamentally different from that of heme systems due to the difficulty in oxidation of non-heme ligands. The experimental descriptions of the high-valent non-heme iron−oxo intermediates must now be developed to evaluate different bonding descriptions and understand reaction pathways.

This address provides a brief overview of our studies in non-heme iron bioinorganic chemistry. A detailed presentation can be found in ref 2. Other areas of research include copper/dioxygen bioinorganic chemistry,[71] blue copper and copper$_A$ centers and their contributions to electron transfer,[72,73] and the electronic structure and bonding in iron sulfur centers.[74] An overview of spectroscopic methods in bioinorganic chemistry is available in ref 75.

Acknowledgment. Throughout the presentation I have referenced individual students and collaborators for their specific contributions discussed. At this point, I would like to express my sincere appreciation to all my graduate students, postdocs, and collaborators who have made my research possible. My students have had the intelligence, creativity, drive, and commitment to solve hard problems and have made my years at Stanford and MIT an awesome experience. My collaborators have allowed me the opportunity to study incredible molecules with limitless resources. My thanks to you, and the NSF and NIH who have provided the funds that have let us solve fundamental problems that do in fact have major health and biotechnological impact. The assistance of Jyllian Kemsley, Andrew Skulan, and Pin-pin Wei in the preparation of this manuscript and the cover art is greatly appreciated.

IC010348A

---

(71) Solomon, E. I.; Chen, P.; Metz, M.; Lee, S.-K.; Palmer, A. E. Submitted for publication.

(72) Solomon, E. I.; Randall, D. W.; Glaser, T. *Coord. Chem. Rev.* **2000**, *200*, 595−632.

(73) Randall, D. W.; Gamelin, D. R.; LaCroix, L. B.; Solomon, E. I. *J. Biol. Inorg. Chem.* **2000**, *5*, 16−29.

(74) Glaser, T.; Hedman, B.; Hodgson, K. O.; Solomon, E. I. *Acc. Chem. Res.* **2000**, *33*, 859−868.

(75) Solomon, E. I.; Hanson, M. A. In *Inorganic Electronic Spectroscopy*; Solomon, E. I., Lever, A. B. P., Eds.; Wiley: New York, 1998; Vol. II, pp 1−129.